Electronic Supplementary Material (ESI) for Energy & Environmental Science.

Developing highly reversible Li-CO_2 battery: from on-chip exploration to practical application

Manman Wang,‡[a] Kai Yang,‡*[ab] Yuchen Ji, ‡[b] Xiaobin Liao,[c] Guangpeng Zhang,[a] Mateus G. Masteghin,[a] Nianhua Peng,[d] Filipe Richheimer,[e] Huanxin Li,[f] Jianan Wang,[g] Xinhua Liu,[h] Shichun Yang,[h] Enrico Petrucco,[i] Paul Shearing,[j] Fernando A. Castro,[ae] S. Ravi P. Silva,[a] Yan Zhao,[c] Feng Pan,*[b] Yunlong Zhao*[aek]

Experimental Section

Materials.

SiO_2 (300 nm) /Si wafer was obtained from Si-Mat Company. Electron-beam (E-beam) source materials (Cr, Ti, Pt, Au, Ag, Cu, Fe, Ni pellet/wire) were purchased from Kurt J. Lesker Company. Li foil (99.9% trace metals basis) was from Thermo Scientific Alfa Aesar. The carbon paper was purchased from Suzhou Sinero Technology Co., Ltd. Bis(trifluoromethane)sulfonimide lithium salt (LiTFSI), Triethylene glycol dimethyl ether (TEGDME) and Whatman® glass microfiber were from Sigma-Aldrich.

On-chip Li-CO_2 batteries fabrication.

The patterned Cr/Au (5 nm/150 nm) and Cr/Cu (5 nm/150 nm), which served as the cathode and anode current collectors, respectively, were first deposited on the 4-inch SiO_2 (300 nm) /Si wafer substrate by Univex E-beam evaporation. The patterned metal films (100 nm of Pt, Au, Ag, Cu, Fe, Ni) with an adhesion layer (10 nm of Ti) were deposited on the substrate as cathode materials via Univex E-beam evaporation. Lithium metal was then deposited on the surface of the patterned anode current collector via a small thermal evaporator (Zhengzhou CY Scientific Instrument Co., Ltd.) which was installed in the Ar glovebox. Three different masks were used in the whole deposition process of the cathode material, current collector, and anode material respectively. The exposed current collectors inside the on-chip LCBs were coated with a thin layer of electrolyte-stable epoxy resin to mitigate potential side reactions or CO_2-related reactions on the current collectors. A glass slide of a certain size covered the cathode and anode materials and was encapsulated by epoxy resin. Two needles were also included within the on-chip battery for electrolyte/CO_2 addition.

Coin cell and pouch cell fabrication

The coin cell and pouch cell were both assembled in the Ar glovebox, in which O_2 and H_2O levels were maintained below 0.1 ppm. For the cathode preparation, 30 nm of Pt was deposited on the carbon paper surface via the Univex E-beam evaporation, the areal mass loading is around 0.1 mg cm^{-2}. 1 M LiTFSI in TEGDME was used as the electrolyte. Glass fibre was served as the separator. Several holes were punched at the coin cell and pouch cell cathode sealing case for CO_2 diffusion. The as-assembled batteries were transferred to the metal-air battery test chamber (Shenzhen Kejing Star Technology Company) for further performance testing.

Material characterizations

Grazing incidence X-ray diffraction (GIXRD) patterns of the metal films were collected by PANalytical X'Pert Pro. The structure and morphology of samples were obtained by field-emission scanning electron microscopy (FESEM, JEOL JSM-7100F), which was equipped with the energy-dispersive X-ray spectroscopy (EDS) detector. Ex situ and in situ Raman spectra were recorded with a Horiba Xplora Plus Confocal Raman Microscope using a 532 nm

wavelength laser and 1800 grating with a 50x long working distance lens. All Raman spectra were intensity normalized to the maximum peak height (maximum normalization). FTIR measurement was conducted on ThermoFisher Scientific, Nicolet iS50. The in situ atomic force microscopy (AFM) observations were conducted inside an argon atmosphere glovebox by a Bruker Multimode 8 system under Scansyst-fluid mode with an insulating silicon nitride tip. The on-chip Li-CO_2 battery is cut off from the silicon wafer and situated at the bottom of the AFM fluid cell. 0.1 mL electrolyte (1 M LiTFSI in TEGDME) is injected into the in-situ cell for each experiment. The electrodes are connected to a GAMRY potentiostat (Gamma 1000) for battery discharge/charge and CV test (Fig S10). The transmission electron microscopy (TEM) images and selected area electron diffractions (SAED) were collected by Talos™ F200i TEM (Thermo Scientific) using a 200 keV electron beam.

Electrochemical measurements

The galvanostatic discharge and charge test, which was used to measure the battery-specific capacity, cyclic stability, energy efficiency and rate performance, was conducted on a NEWARE battery tester (CT-4008Q-5 V100 mA). Cyclic voltammetry (CV) was measured with a GAMRY potentiostat (Gamma 1000). The energy density of the Li-CO_2 coin cells was calculated by the using the recorded discharging energy (final discharging state) dividing the catalyst weight of per electrode.

Computational methods

The first-principle calculations were conducted within the density functional theory (DFT) through the Vienna ab-initio Simulation Package (VASP). The Perdew-Burke-Ernzerhof (PBE) exchange-correlation functional within the generalized gradient approximation was employed. The cut-off energy for the kinetic energy was set to 520 eV and a 3×3×1 Monkhorst-Pack k-mesh was applied for sampling in the Brillouin zone. The energy convergence tolerance and the force certification were set as 1×10^{-5} eV/atom and 0.02 eV/Å, respectively. The DFT-D3 method with Becke-Jonson (BJ) damping was used for the Van der Waals (vdW) corrections. The absorption calculations were performed in the (111) plane of Pt. The general adsorption energies (E_{ads}) were obtained through the following equation: $E_{ads} = E_{substrate\text{-}adsorbate} - E_{substrate} - E_{adsorbate}$, where $E_{substrate\text{-}adsorbate}$, $E_{substrate}$, $E_{adsorbate}$ represent the total energy of the substrate with adsorbed species, the substrate, and the molecule/atom (e.g., CO_2, Li, Li_2CO_3), respectively. The Gibbs free energy change (ΔG) was calculated based on the following equation: $\Delta G = \Delta E + \Delta ZPE - T\Delta S$, where ΔE is the reaction energy change, T is the temperature (298.15 K), ΔZPE and ΔS denote the change in zero-point-energy and entropy, respectively.

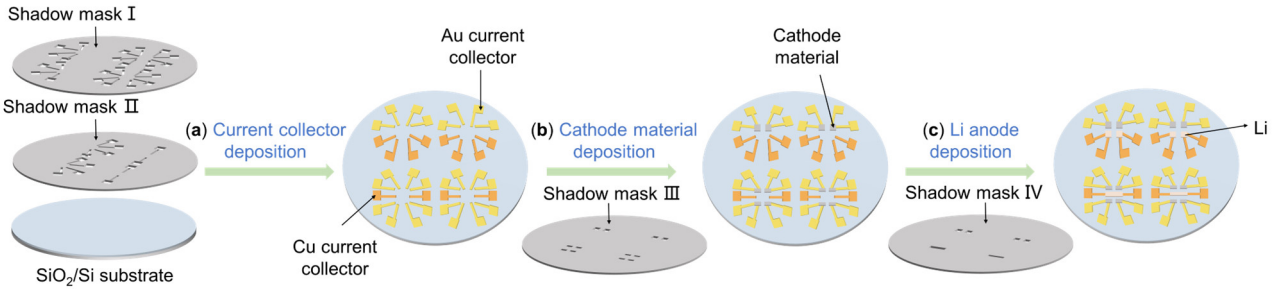

Fig S1 Schematic of on-chip Li-CO_2 batteries fabrication process. The (a) current collector, (b) cathode material, and (**c**) anode material are deposited on a 4-inch wafer in sequence.

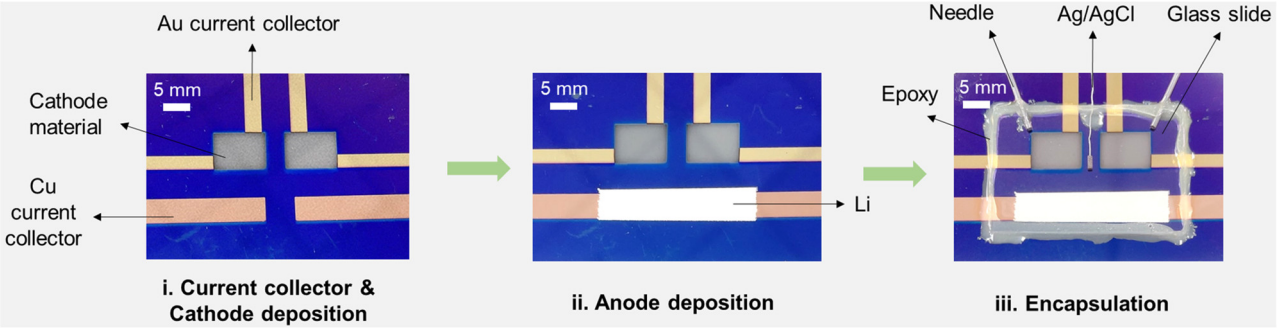

Fig S2 Images of on-chip Li-CO_2 devices at different fabrication steps: (i) after current collector and cathode material deposition, (ii) after anode deposition, (iii) after device encapsulation.

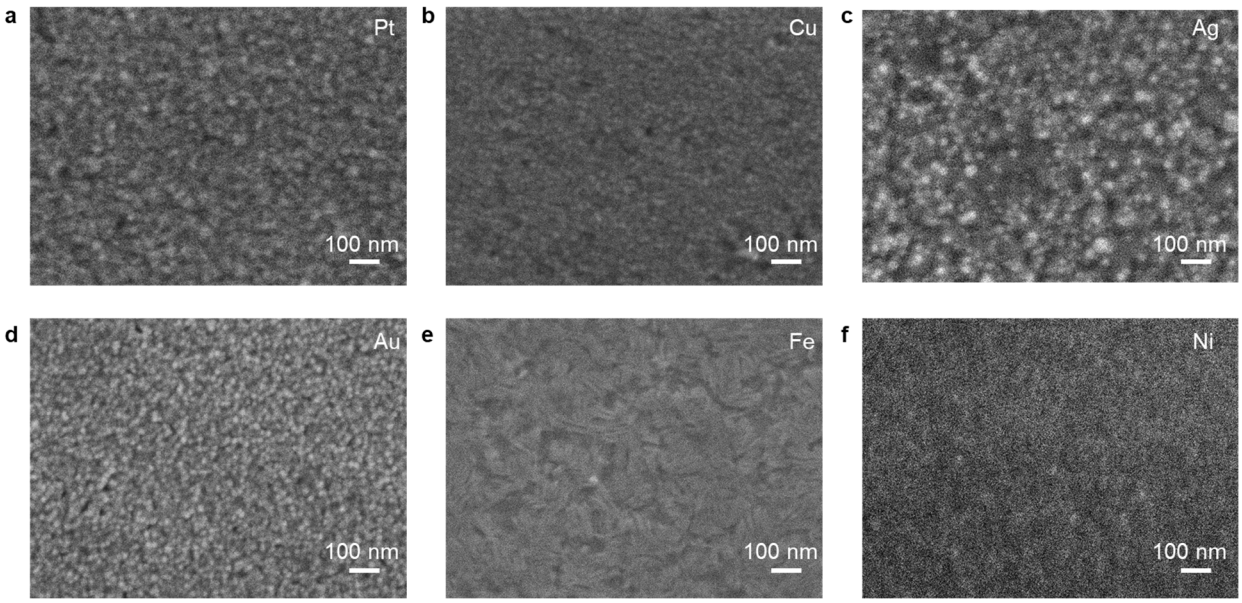

Fig S3 Scanning electron microscopy (SEM) images of deposited six different cathode films with the thickness of 100 nm on SiO_2/Si wafer: (**a**) Pt, (**b**) Cu, (**c**) Ag, (**d**) Au, (**e**) Fe, and (**f**) Ni. In order to improve the film quality of the cathode material, a 10-nm-thick adhesion layer was first deposited before the cathode material was evaporated.

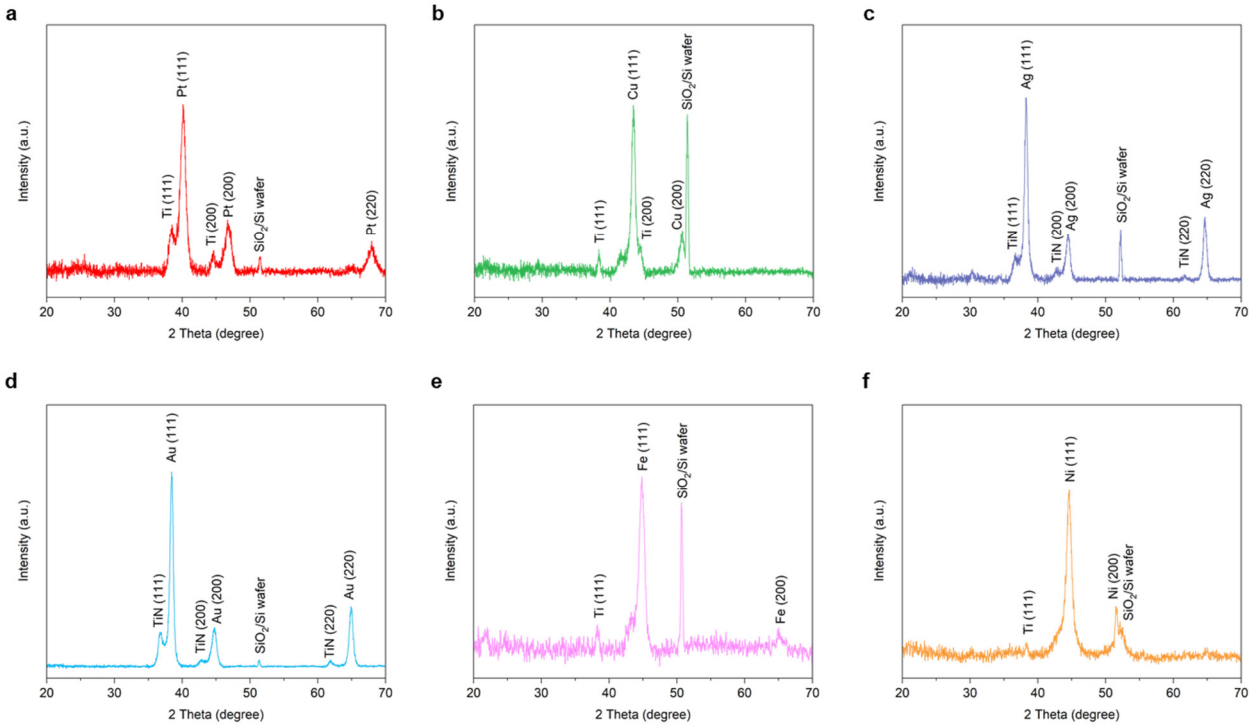

Fig S4 The X-ray diffraction (XRD) pattern of deposited six different cathode films with the thickness of 100 nm on SiO_2/Si wafer: (**a**) Pt, (**b**) Cu, (**c**) Ag, (**d**) Au, (**e**) Fe, and (**f**) Ni. In order to improve the film quality of the cathode material, a 10-nm-thick adhesion layer was first deposited before the cathode material was evaporated.

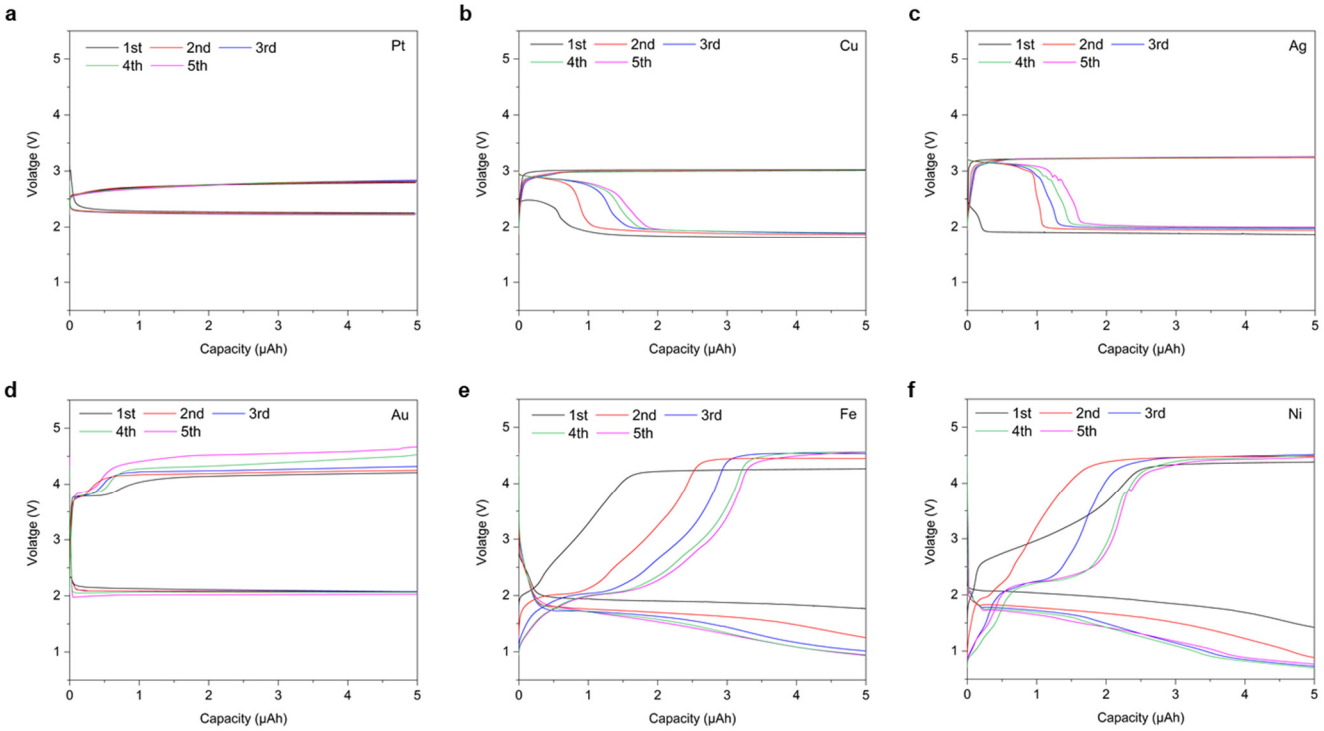

Fig S5 On-chip Li-CO_2 batteries electrochemical performances comparison. Discharge-charge curves of different cathode materials with a limit capacity of 5 μAh at the constant current of 1 μA: (**a**) Pt, (**b**) Cu, (**c**) Ag, (**d**) Au, (**e**) Fe, and (**f**) Ni.

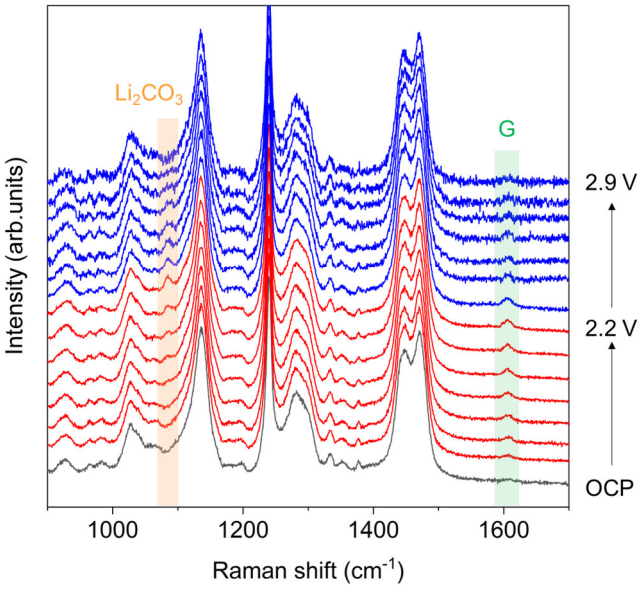

Fig S6 In situ Raman spectra of Pt cathode recorded during the corresponding Galvanostatic discharge-charge process. Black, red, and blue curves represent the battery in open circuit potential state (OCP), discharge state, and charge state, respectively.

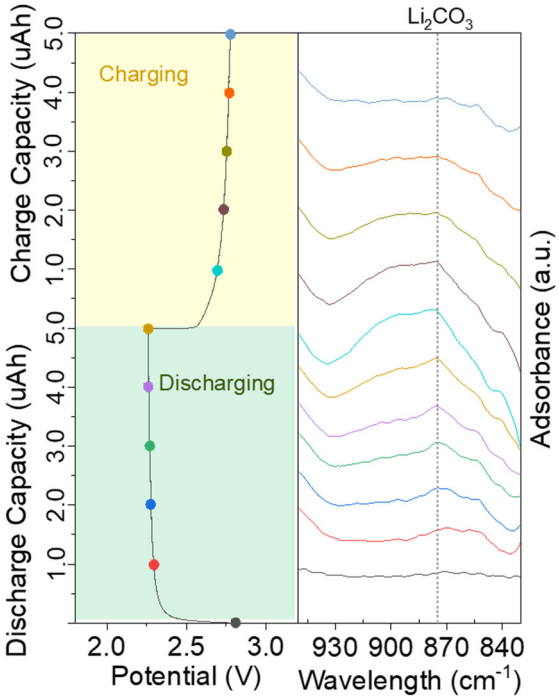

Fig S7 In situ FTIR measurement of the Pt-based on-chip LCBs.

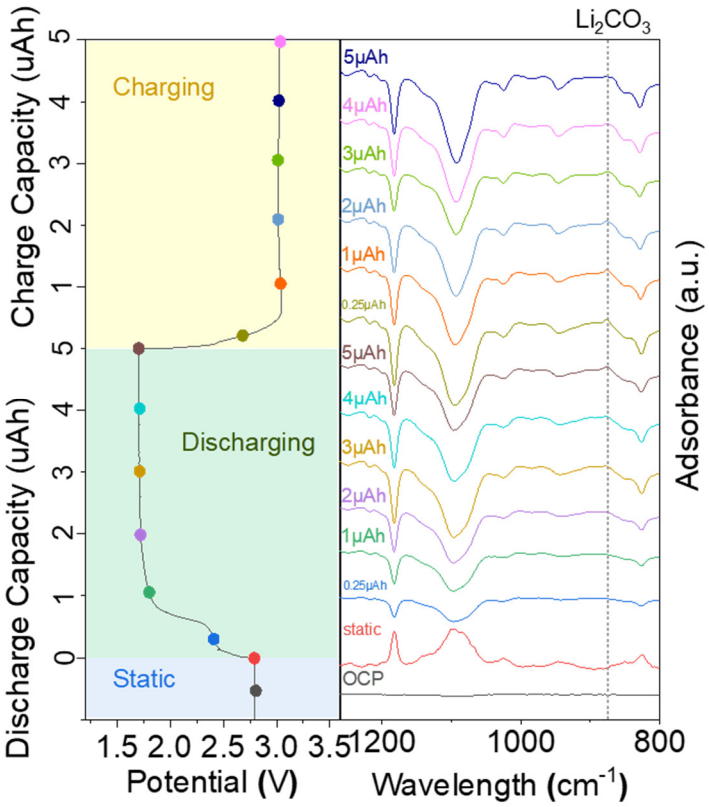

Fig S8 In situ FTIR measurement of the Cu-based on-chip LCBs.

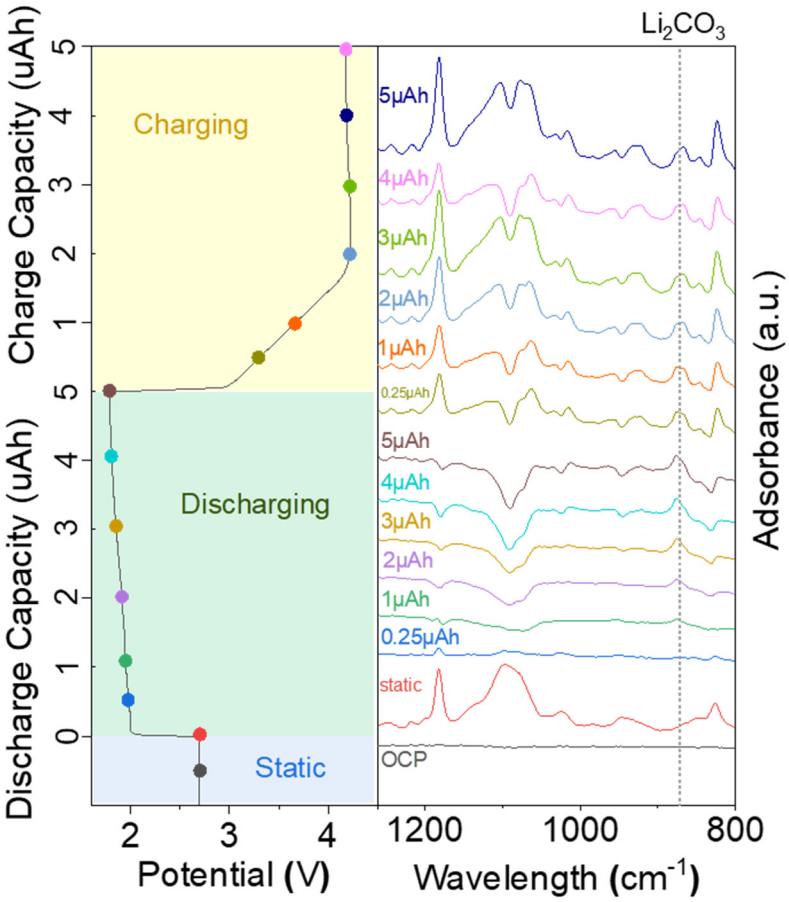

Fig S9 In situ FTIR measurement of the Ni-based on-chip LCBs.

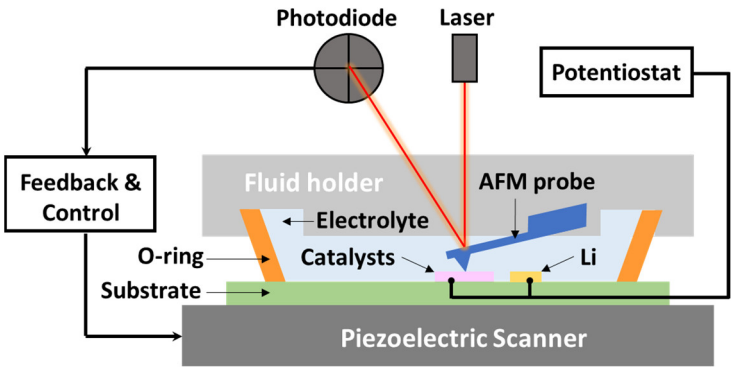

Fig S10. The schematic diagram of the on-chip in situ AFM setup.

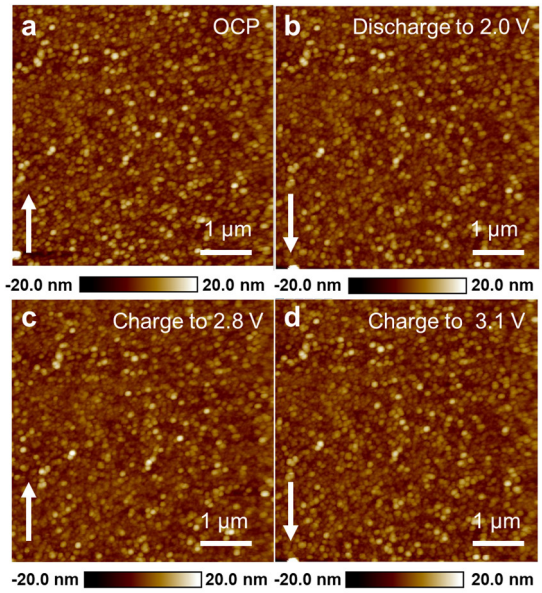

Fig S11 In situ atomic force microscopy (AFM) images of Pt cathode in Ar atmosphere obtained at (**a**) OCP, (**b**) discharge to 2.0 V, (**c**) charge to 2.8 V, and (**d**) charge to 3.1 V. The white arrows represent the scanning direction.

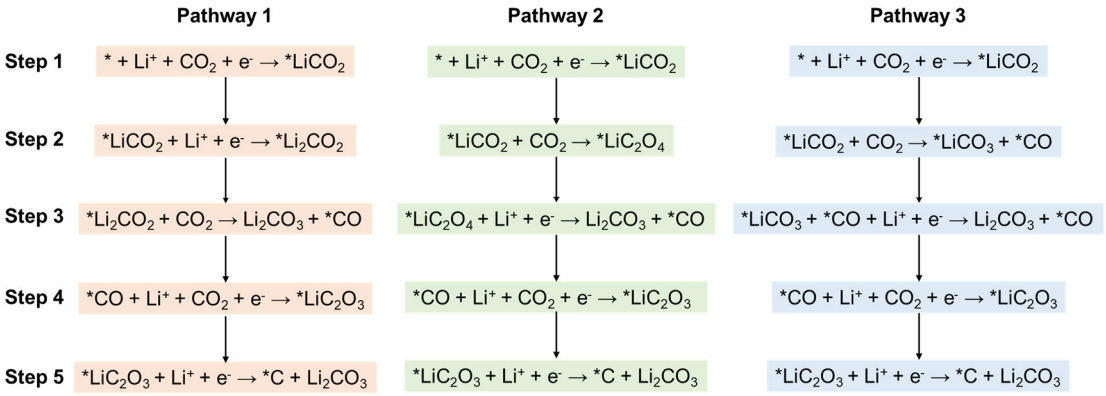

Fig S12 Three possible reaction pathways for the formation of C and Li_2CO_3. The * represents the basal plane of Pt(111).

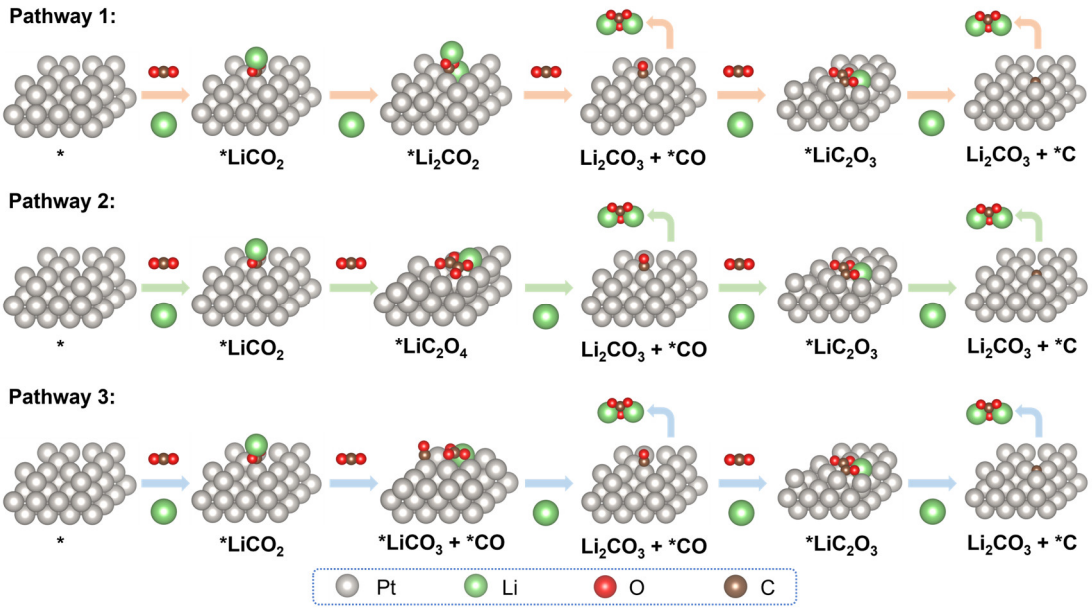

Fig S13 The schematic of three reaction pathways and the optimized structures of reactants and intermediates. * represents the Pt(111) substrate.

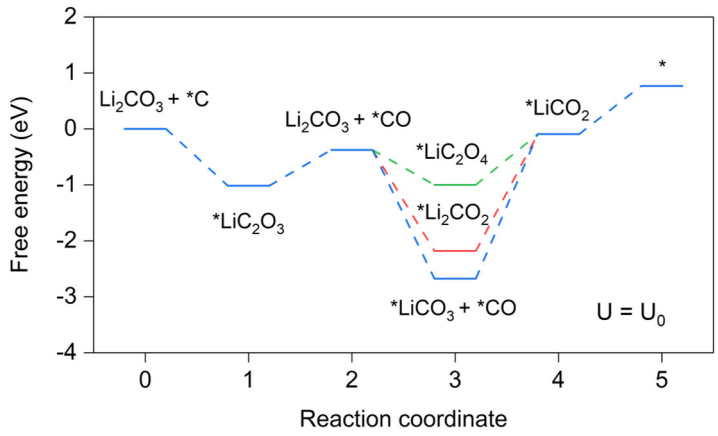

Fig S14 Gibbs free energy diagram of three different reaction pathways on Pt(111) surface during charge process at $U = U_0 = 2.85$ V.

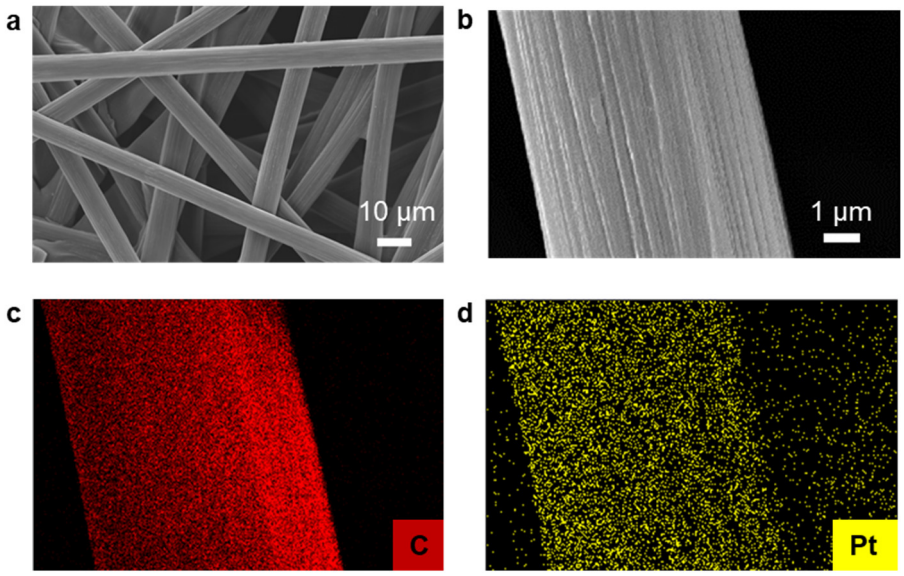

Fig S15 (a) SEM image of Pt@carbon paper (Pt@CP). (**b-d)**, EDS elemental mappings of carbon (red) and Pt (yellow).

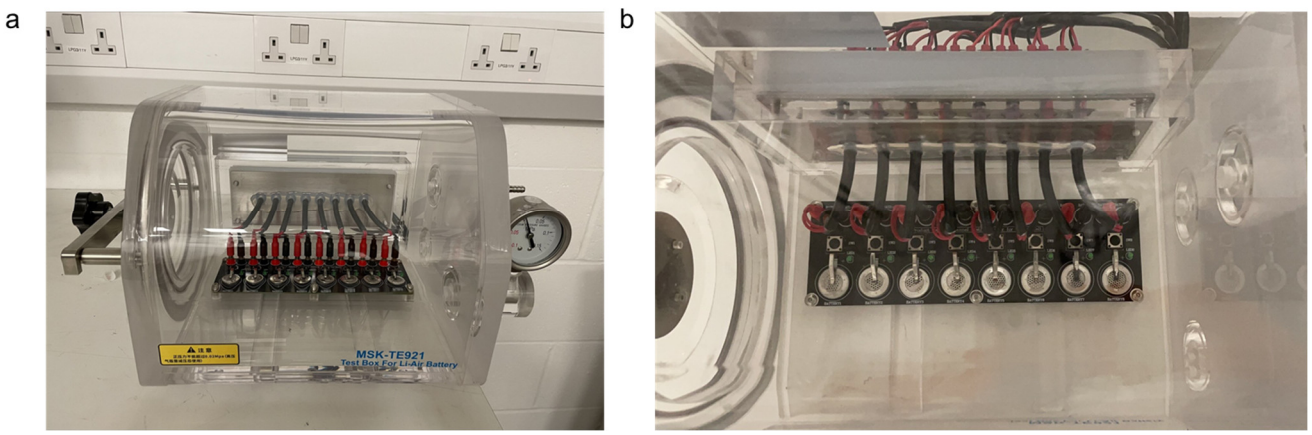

Fig S16 Images of commercial Li-CO_2 battery test box: (**a**) front view, (**b**) top view.

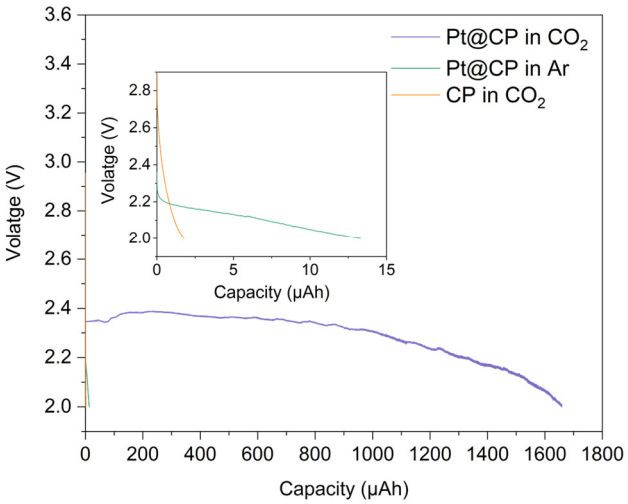

Fig S17 Full discharge curves of carbon paper (CP) and Pt@CP based Li-CO_2 coin cell in the CO_2 and Ar atmosphere at the same constant current. The inset is the enlarged image of the full discharge curve for Pt@CP in the Ar atmosphere and CP in the CO_2 atmosphere.

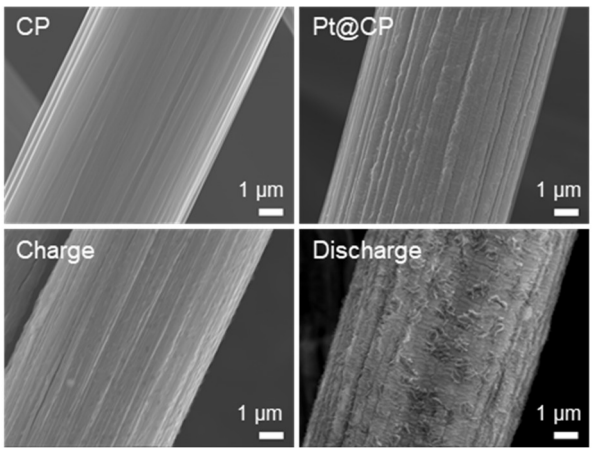

Fig S18 SEM images of pure CP, pristine Pt@CP, Pt@CP after discharging and Pt@CP after recharging.

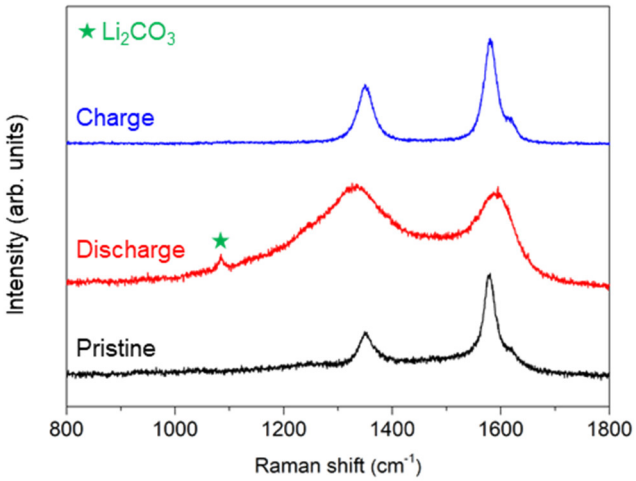

Fig S19 Raman spectra of Pt@CP at pristine state, after discharging state and after recharging state.

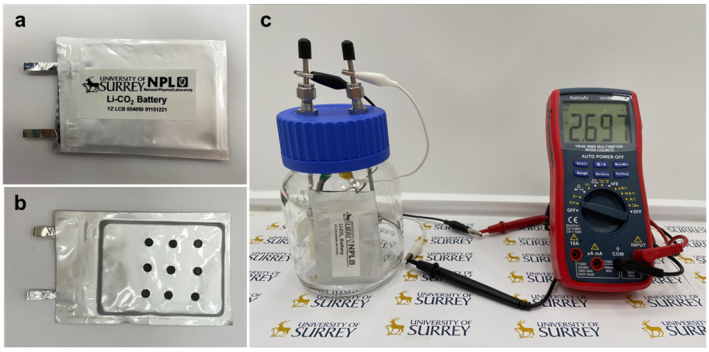

Fig S20 Photographs of the assembled Pt-based Li-CO_2 pouch cell: front side (**a**) and back side (**b**). **c**, Photograph of the assembled Pt-based Li-CO_2 pouch cell inside the testing bottle which is full of CO_2. The pouch cell is also connected to a multimeter for OCP measurement.

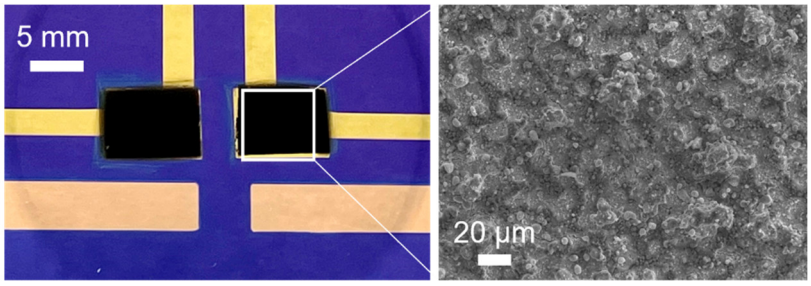

Fig S21 Spray coating porous activated carbon on the on-chip devices: optical images (left) and SEM images (right).

For the demonstration of practical high loading of catalyst and carbon material as current collector, we used the spray coating techniques to load activated carbon (AC). The porous activated carbon (AC, specific surface ~ 2000 m^2 g^{-1}) was mixed with carbon black and polyvinyl pyrrolidone (PVP) in isopropanol. A uniformly dispersed slurry can be obtained after ultrasonic dispersion. The slurry can be further spray-coated onto the on-chip devices with tailored mask and the electrode thickness can be controlled. After vacuum drying, the working electrode can be uniformly covered by the carbon material as current collectors. The areal mass loading of the AC-based on-chip LCB is around 0.5 mg cm^{-2} which is at the common level compared with literature. By physically mixing different catalyst with the carbon material slurry or chemically synthesizing catalyst onto the AC and then spray coating onto the devices, a configuration of catalyst on carbon material substrate can be achieved.

The electrochemical testing result is shown in the **Fig S22** which confirms its functionality under high mass loading of catalyst. **Fig S23** displays the Raman measurement of the AC-based on-chip devices before cycling, typical Raman spectra of activated carbon can be clearly observed.

In summary, the demonstrated on-chip platform can be also used for a wide range of catalyst with high loading and deliver integrated test and analysis functions.

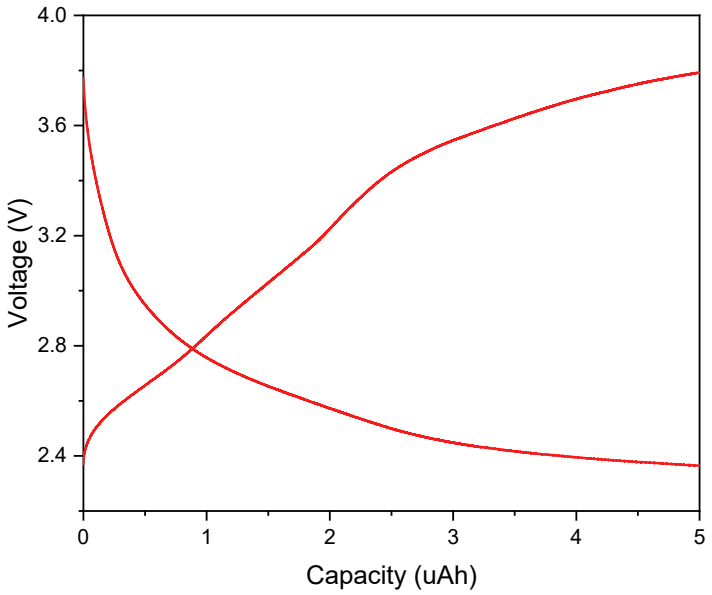

Fig S22. Voltage curve of the AC-based on-chip LCB.

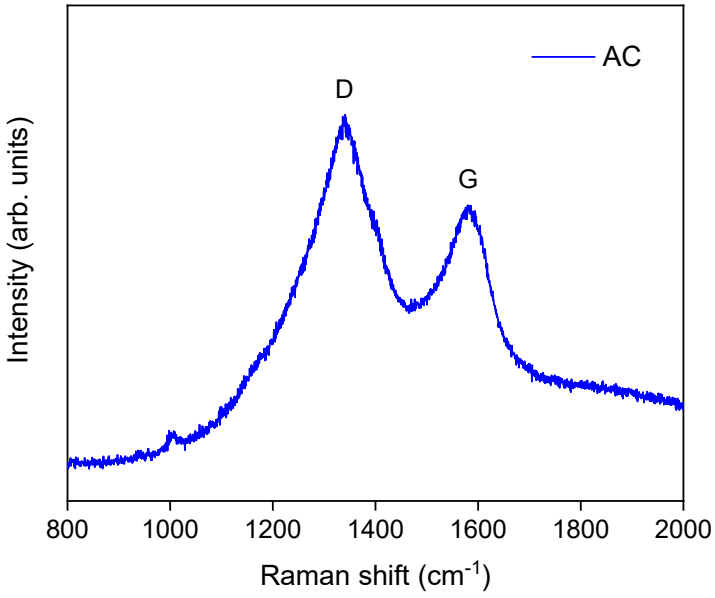

Fig S23. Raman measurement of the AC-based on-chip LCB (before cycling).

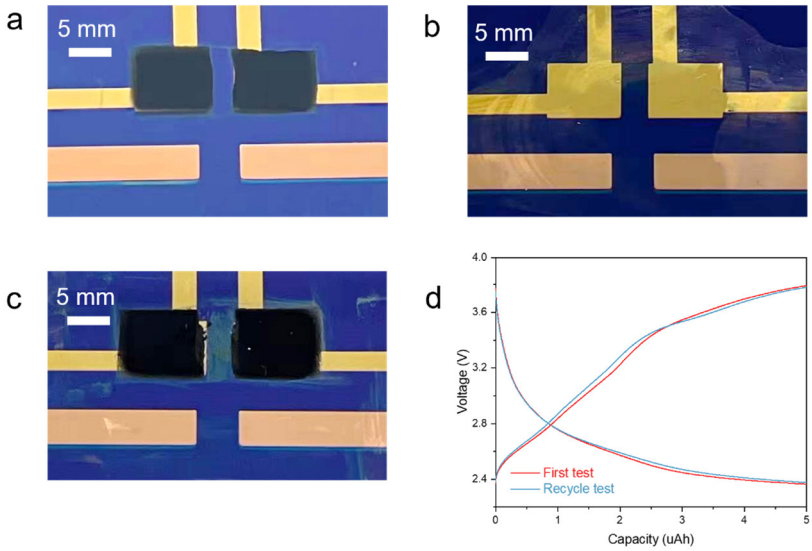

Fig S24. Recycling test of the on-chip Li-CO_2 platform. (a) Digital image of on-chip LCB with spray coating AC as cathode electrode. (b) Digital image of the washed platform after testing. (c) Repeated coating the platform with activated carbon. (d) Voltage-curves of the first test and recycle test on the same platform.

For the demonstration of recycling utilization of the on-chip platform, AC was coated onto the on-chip platform (**Fig S24a**) and the AC-based on-chip LCB was further fabricated in the glovebox according to the procedures in **Experimental Section**. Ultraviolet polymerization glue was used to seal the batteries for better fabrication and disassembling. After electrochemical testing, the on-chip platform was disassembled and washed with isopropanol and ethanol. The surface of the on-chip platform was refreshed, and the current collectors also remained stable as shown in **Fig S24b**. The AC electrode slurry was spray-coated onto the platform again (**Fig S24c**) and the corresponding on-chip LCB was tested under the same conditions. The electrochemical performance of the two LCBs was compared as shown in the **Fig S24d**. The almost overlapped voltage curves confirmed that the recyclability of the on-chip platform.

Table S1 Electrochemical performance comparison of Li-CO_2 batteries with different cathode catalysts.

	Electrolyte	Discharge/charge voltage	Over-potential	Energy efficiency	Discharge capacity	Stability	Ref
IrRu/N-CNT	1 M LiTFSI/TEGDME	2.6 V / 3.8 V (500 mAh/g @ 100 mA/g)	1.2 V	*68.4%	6228 mAh/g (100 mA/g, 2 V)	600 cycles (2.5-4.2 V, 500 mAh/g @ 100 mA/g)	2023, Adv. Funct. Mater., DOI: 10.1002/adfm.202213931[1]
Sn$Cu_{1.5}O_{3.5}$@MFI	1 M LiTFSI/TEGDME	2.34 V / 4.02 V (1000 mAh/g @ 100 mA/g)	1.68 V	*58.2%	23000 mAh/g (100 mA/g, 2 V)	100 cycles (2.25-4.75 V, 1000 mAh/g @ 100 mA/g)	2023 Adv. Eng. Mater., DOI: 10.1002/aenm.202204143[2]
Cd SAs/NC	1 M LiTFSI/DMSO containing 0.3 M $LiNO_3$	2.91 V / 4.22 V (1000 mAh/g @ 200 mA/g)	1.31 V	*70%	160045 mAh/g (500 mA/g, 2 V)	1685 cycles (2.5-4.5 V, 500 mAh/g @ 1 A/g)	2023, Adv. Funct. Mater., DOI: 10.1002/adfm.202213841[3]
TiVC/rGO aerogels (TVGA)	1 M $LiCF_3SO_3$-TEGDME	2.77 V / 4.18 V (1000 mAh/g @ 100 mA/g)	1.41 V	*66.3%	27880 mAh/g (100 mA/g, 2 V)	91 cycles (2.5-4.5 V, 1000 mAh/g @ 200 mA/g)	2023, Adv. Funct. Mater., DOI: 10.1002/adfm.202210037[4]
Fe NPs@N-CNTs	1 M LiTFSI/TEGDME	2.6 V / 4.25 V (600 mAh/g_{carbon} @ 100 mA/g_{carbon})	1.65 V	*61.2%	3898 mAh/g (100 mA/g_{carbon}, 2.3 V)	30 cycles (2.5-4.5 V), 600 mAh/g_{carbon} @ 100 mA/g_{carbon}	2021, ACS Mater. Lett., DOI: 10.1021/acsmaterialslett.1c00078[5]

Ru atomic cluster & single atom **Ru-N_4** composite / carbon nanobox	1 M LiTFSI/TEGDME	3.01 V / 4.06 V (1000 mAh/g @ 100 mA/g)	1.05 V	*74.1%	10651.9 mAh/g (100 mA/g, 2 V)	62 cycles (2.5-4.5 V, 500 mAh/g @ 300 mA/g)	2022, Adv. Mater., DOI: 10.1002/adma.202200559[6]
Ni/Ru core/shell hexagonal nanoplate/VC72	1 M LiTFSI/TEGDME	2.87 V / 3.75 V (1000 mAh/g @ 200 mA/g)	0.88 V	*76.5%	~10000 mAh/g (200 mA/g, 2 V)	120 cycles (2.4-4.2 V, 1000 mAh/g @ 200 mA/g)	2022, Adv. Mater., DOI: 10.1002/adma.202204134[7]
Ru-Co Nanosheets/CNT	1 M LiTFSI/DMSO containing 0.3 M $LiNO_3$	2.8 V / 3.74 V (1000 mAh/g @ 100 mA/g)	0.94 V	75%	8057 mAh/g (100 mA/g, 2 V)	43 cycles (2.4-4.5 V, 500 mAh/g @ 250 mA/g)	2022, Adv. Funct. Mater., DOI: 10.1002/adfm.202202737[8]
MnOx-CeO_2@Polypyrrole	1 M $LiCF_3SO_3$/TEGDME	2.64 V / 4.13 V (1000 mAh/g @ 100 mA/g)	1.49 V	*63.9%	13631 mAh/g (100 mA/g, 2 V)	253 cycles (2.3-4.25 V, 1000 mAh/g @ 100 mA/g)	2022 Adv. Eng. Mater., DOI: 10.1002/aenm.202103667[9]
Single-Atom **Ru-Co_3O_4** Nanosheets/ carbon cloth	1 M LiTFSI/TEGDME	2.75 V / 3.8 V (500 mAh/g @ 100 mA/g)	1.05 V	*72%	30915 mAh/g (100 mA/g, 2 V)	200 cycles (2.6-4.1 V, 800 mAh/g @ 200 mA/g)	2021, Adv. Sci., DOI: 10.1002/advs.202102550[10]
W_2C nanoparticles/CNTs	1 M $LiClO_4$/ DMSO	2.9 V / 4.1 V (500 mAh/g @ 200 mA/g)	1.2 V	*70.7%	10632 mAh/g (100 mA/g, 2.5 V)	75 cycles (2.9-4.1 V, 500 mAh/g @ 200 mA/g)	2021, ACS Energy Lett., DOI: 10.1021/acsenergylett.1c01428[11]
Ru/Co-CPY@CNT-2	1 M LiTFSI/TEGDME	3.06 V/ 3.90 V (1000 mAh/g @ 100 mA/g)	0.84 V	*78%	24740 mAh/g (200 mA/g, 2 V)	180 cycles (2.5-4.5 V, 1000 mAh/g @ 500 mA/g)	2021, Cell Rep. Phys. Sci., DOI: 10.1016/j.xcrp.2021.100583[12]

Hierarchical **$Ti_3C_2T_x$** MXene/Carbon Nanotubes	1 M LiTFSI/TEGDME	2.74 V/ 4.15 V (1000 mAh/g @ 200 mA/g)	1.41 V	*66%	11458 mAh/g (500 mA/g, 2 V)	100 cycles (2.25-4.3 V, 1000 mAh/g @ 200 mA/g)	2021, ACS Nano, DOI: 10.1021/acsnano.0c10558[13]
Graphdiyne/KB hybird	1 M LiTFSI/TEGDME	2.77 V/ 4.17 V (1000 mAh/g @ 50 mA/g)	≈1.4 V	*66.4%	18416 mAh/g (100 mA/g, 2 V)	158 cycles (2.2-4.7 V, 1000 mAh/g @ 400 mA/g)	2021, Adv. Funct. Mater., DOI: 10.1002/adfm.202101423[14]
Single **Fe** atoms / N,S-codoped holey graphene sheets	1 M LiTFSI/DMSO containing 0.3 M $LiNO_3$	2.78 V / 3.95 V (1000 mAh/g @ 100 mA/g)	≈1.17 V	*70.3%	23174 mAh/g (100 mA/g, 2.2 V)	200 cycles (2.5-4.4 V, 1000 mAh/g @ 1 A/g)	2020, Adv. Mater., DOI: 10.1002/adma.201907436[15]
Ru nanoparticles / N,S-codoped graphene	1 M LiTFSI/TEGDME	2.91 V / 4.04 V (1000 mAh/g @ 100 mA/g)	1.13 V	*72%	12448 mAh/g (100 mA/g, 2 V)	100 cycles (2.6-4.0 V, 1000 mAh/g @ 100 mA/g)	2020, Energy Storage Mater., DOI: 10.1016/j.ensm.2020.01.021[16]
RuRh Nanosheet / VC72	1 M LiTFSI/DMSO	≈2.8 V / ≈3.8 V (1000 mAh/g @ 200 mA/g)	≈1 V	*70.4%	9600 mAh/g (200 mA/g, 2.2 V)	180 cycles (2.25-3.95 V, 1000 mAh/g @ 200 mA/g)	2020, Matter, DOI: 10.1016/j.matt.2020.02.020[17]
Adjacent **Co** atoms / Graphene oxide	1 M LiTFSI/TEGDME	≈2.51 V / ≈4.15 V (1000 mAh/g @ 100 mA/g)	≈1.63 V	*60.5%	17358 mAh/g (100 mA/g, 2 V)	100 cycles (2.4-4.2 V, 1000 mAh/g @ 100 mA/g)	2019, Adv. Funct. Mater., DOI: 10.1002/adfm.201904206[18]
Ru-Cu nanoparticles / Graphene	1 M LiTFSI/TEGDME	≈2.7 V / ≈3.5 V (1000 mAh/g @ 200 mA/g)	<0.88 V	67.9% (200 mA/g)	13698 mAh/g (200 mA/g, 2.2 V)	100 cycles (2.7-3.6 V, 1000 mAh/g @ 200 mA/g)	2019 Adv. Eng. Mater. DOI: 10.1002/aenm.201802805[19]

Ir nanosheets / N-doped carbon nanofibers	1 M LiTFSI/TEGDME	2.75 V / 3.8 V (1000 mAh/g @ 100 mA/g)	1.05 V	*72.3%	7666.7 mAh/g (166.7 mA/g, 2 V)	150 cycles (2.6-3.9 V, 1000 mAh/g @ 200 mA/g)	2018, Adv. Mater., DOI: 10.1002/adma.201803124[20]
Ni nanoparticles/ N-doped graphene	1 M LiTFSI/TEGDME	≈2.82 V / ≈4.25 V (1000 mAh/g @ 100 mA/g)	≈1.43 V	*66.4%	17625 mAh/g (100 mA/g, 2.2 V)	100 cycles (2.5-4.2 V, 1000 mAh/g @ 100 mA/g)	2018, Adv. Sci., DOI: 10.1002/advs.201700567[21]
Cu nanoparticles / N-doped graphene	1 M LiTFSI/TEGDME	≈2.8 V / ≈3.8 V (1000 mAh/g @ 200 mA/g)	≈1 V	*70.4%	14864 mAh/g (200 mA/g, 2.2 V)	50 cycles (2.5-4.0 V, 1000 mAh/g @ 200 mA/g)	2018, J. Mater. Chem. A, DOI: 10.1039/C7TA10497A[22]
Ru@Super P	$LiCF_3SO_3$–TEGDME (mole ratio of 1 : 4)	2.54 V / 4.25 V (1000 mAh/g @ 100 mA/g)	1.71 V	71% (65 cycles)	8229 mAh/g (100 mA/g, 2 V)	80 cycles (2.5-4.4 V, 1000 mAh/g @ 100 mA/g)	2017, Energy Environ. Sci., DOI: 10.1039/c6ee03770d[23]
Pt	1 M LiTFSI/TEGDME	2.56 V/ 2.91 V (1000 mAh/g @ 100 mA/g)	**~0.35 V**	**89.5%** (100 mA/g)	**41466 mAh/g** (100 mA/g, 2 V)	100 cycles (2.2-3.1 V, 1000 mAh/g @ 200 mA/g)	**Our work**

* denotes the energy efficiency value calculated from performance data reported in the literature.

Table S2 The Gibbs free energy change (ΔG) of each reaction step on the basal plane of Pt(111).

Reaction step on Pt(111)	**Pathway 1**	**Pathway 2**	**Pathway 3**
(1) ΔG (eV, $U=U_0$=2.85 V)	-0.86	-0.86	-0.86
(2) ΔG (eV, $U=U_0$=2.85 V)	-2.09	-0.914	-2.58
(3) ΔG (eV, $U=U_0$=2.85 V)	1.80	0.62	2.30
(4) ΔG (eV, $U=U_0$=2.85 V)	-0.64	-0.64	-0.64
(5) ΔG (eV, $U=U_0$=2.85 V)	1.01	1.01	1.01

Table S3. Summary of suitable catalysts loading techniques for the demonstrated platform.

Methods	Materials	Catalyst engineering	Ref
Thermal evaporation	Most compounds and elements	The internal temperature, pressure and evaporation rate, substrate temperature, annealing	Materials Today Advances, 2022, **14**, 100232[24]
Spin-coating	Compounds that are readily soluble or dispersible	Dispense volume, solution viscosity, solution concentration, spin time	Indian J Phys, 2009, **83**, 493–502[25]
Electrodeposition	Pure metals and alloys	Deposition current and deposition time	Russ J Electrochem, 2016, **52**, 806–831[26]
Spraying	Nanoscale to microscale particles	Spray distance, carrier gas flow rate, spray time	Surface and Coatings Technology, 2008, **202**, 4483–4490[27]
On-chip self -assembly	Colloidal particles, block copolymers, nano particles	External fields, evaporation, surface tension and interface interaction	Advances in Colloid and Interface Science, 2018, **251**, 97–114[28]
Ion Implantation	Metals, polymers, semiconductors.	Ion energy, post-implantation annealing	Sensors, 2018, **18**, 2358[29]
Chemical vapor deposition	Precious metals, semiconductors	Deposition temperature, substrate choice, pressure and gas flow	Materials, 2018, **11**, 822[30]

References

1. Wang, Z. et al. Dual Catalytic Sites of Alloying Effect Bloom CO_2 Catalytic Conversion for Highly Stable Li–CO_2 Battery. *Adv. Funct. Mater.* **n/a**, 2213931 (2023).
2. Zhu, Y. et al. Confinement of $SnCu_xO_{2+x}$ Nanoclusters in Zeolites for High-Efficient Electrochemical Carbon Dioxide Reduction. *Adv. Energy Mater.* **13**, 2204143 (2023).
3. Zhu, K. et al. Single-Atom Cadmium-N_4 Sites for Rechargeable Li–CO_2 Batteries with High Capacity and Ultra-Long Lifetime. *Adv. Funct. Mater.* **33**, 2213841 (2023).
4. Zhao, W. et al. Toward an Understanding of Bimetallic MXene Solid-Solution in Binder-Free Electrocatalyst Cathode for Advanced Li–CO_2 Batteries. *Adv. Funct. Mater.* **33**, 2210037 (2023).
5. Kim, H.-S., Lee, J.-Y., Yoo, J.-K. & Ryu, W.-H. Capillary-Driven Formation of Iron Nanoparticles Embedded in Nanotubes for Catalyzed Lithium–Carbon Dioxide Reaction. *ACS Materials Letters* **3**, 815-825 (2021).
6. Lin, J. et al. Boosting Energy Efficiency and Stability of Li–CO_2 Batteries via Synergy between Ru Atom Clusters and Single-Atom Ru–N_4 sites in the Electrocatalyst Cathode. *Adv. Mater.* 2200559 (2022).
7. Fan, L. et al. Biaxially Compressive Strain in Ni/Ru Core/Shell Nanoplates Boosts Li–CO_2 Batteries. *Adv. Mater.* **34**, 2204134 (2022).
8. Wang, Y. et al. Decreasing the Overpotential of Aprotic Li-CO_2 Batteries with the In-Plane Alloy Structure in Ultrathin 2D Ru-Based Nanosheets. *Adv. Funct. Mater.* **32**, 2202737 (2022).
9. Deng, Q. et al. Electronic State Modulation and Reaction Pathway Regulation on Necklace-Like MnO_x-CeO_2@Polypyrrole Hierarchical Cathode for Advanced and Flexible Li–CO_2 Batteries. *Adv. Energy Mater.* **12**, 2103667 (2022).
10. Lian, Z. et al. Single-Atom Ru Implanted on Co_3O_4 Nanosheets as Efficient Dual-Catalyst for Li-CO_2 Batteries. *Adv. Sci.* **8**, 2102550 (2021).
11. Zhang, X. et al. Breaking the Stable Triangle of Carbonate via W–O Bonds for Li-CO_2 Batteries with Low Polarization. *ACS Energy Lett.* **6**, 3503-3510 (2021).
12. Wang, J.-H. et al. Single-metal site-embedded conjugated macrocyclic hybrid catalysts enable boosted CO_2 reduction and evolution kinetics in Li-CO_2 batteries. *Cell Rep. Phys. Sci.* **2**, 100583 (2021).
13. Hu, Z. et al. Hierarchical $Ti_3C_2T_x$ MXene/Carbon Nanotubes for Low Overpotential and Long-Life Li-CO_2 Batteries. *ACS Nano* **15**, 8407-8417 (2021).
14. Zhang, J. et al. Rechargeable Li–CO_2 Batteries with Graphdiyne as Efficient Metal-Free Cathode Catalysts. *Adv. Funct. Mater.* **31**, 2101423 (2021).
15. Hu, C. et al. High-Performance, Long-Life, Rechargeable Li–CO_2 Batteries based on a 3D Holey Graphene Cathode Implanted with Single Iron Atoms. *Adv. Mater.* **32**, 1907436 (2020).
16. Qiao, Y. et al. Synergistic effect of bifunctional catalytic sites and defect engineering for high-performance Li–CO_2 batteries. *Energy Storage Mater.* **27**, 133-139 (2020).

17. Xing, Y. et al. Ultrathin RuRh Alloy Nanosheets Enable High-Performance Lithium-CO_2 Battery. *Matter* **2**, 1494-1508 (2020).
18. Zhang, B.-W. et al. Targeted Synergy between Adjacent Co Atoms on Graphene Oxide as an Efficient New Electrocatalyst for Li–CO_2 Batteries. *Adv. Funct. Mater.* **29**, 1904206 (2019).
19. Zhang, Z. et al. Exploiting Synergistic Effect by Integrating Ruthenium–Copper Nanoparticles Highly Co-Dispersed on Graphene as Efficient Air Cathodes for Li–CO_2 Batteries. *Adv. Energy Mater.* **9**, 1802805 (2019).
20. Xing, Y. et al. Crumpled Ir Nanosheets Fully Covered on Porous Carbon Nanofibers for Long-Life Rechargeable Lithium–CO_2 Batteries. *Adv. Mater.* **30**, 1803124 (2018).
21. Zhang, Z. et al. Verifying the Rechargeability of Li-CO_2 Batteries on Working Cathodes of Ni Nanoparticles Highly Dispersed on N-Doped Graphene. *Adv. Sci.* **5**, 1700567 (2018).
22. Zhang, Z. et al. Identification of cathode stability in Li–CO_2 batteries with Cu nanoparticles highly dispersed on N-doped graphene. *J. Mater. Chem. A* **6**, 3218-3223 (2018).
23. Yang, S. et al. A reversible lithium–CO_2 battery with Ru nanoparticles as a cathode catalyst. *Energy Environ. Sci.* **10**, 972-978 (2017).
24. Bae, S. R., Heo, D. Y. & Kim, S. Y. Recent progress of perovskite devices fabricated using thermal evaporation method: Perspective and outlook. *Materials Today Advances* **14**, 100232 (2022).
25. Sahu, N., Parija, B. & Panigrahi, S. Fundamental understanding and modeling of spin coating process: A review. *Indian J. Phys.* **83**, 493-502 (2009).
26. Davydov, A. D. & Volgin, V. M. Template electrodeposition of metals. Review. *Russ. J. Electrochem.* **52**, 806-831 (2016).
27. Pierlot, C., Pawlowski, L., Bigan, M. & Chagnon, P. Design of experiments in thermal spraying: A review. *Surf. Coat. Technol.* **202**, 4483-4490 (2008).
28. van Dommelen, R., Fanzio, P. & Sasso, L. Surface self-assembly of colloidal crystals for micro- and nano-patterning. *Adv. Colloid Interface Sci.* **251**, 97-114 (2018).
29. Teranishi, N., Fuse, G. & Sugitani, M. A Review of Ion Implantation Technology for Image Sensors †. *Sensors*; 2018.
30. Manawi, Y. M., Ihsanullah, Samara, A., Al-Ansari, T. & Atieh, M. A. A Review of Carbon Nanomaterials' Synthesis via the Chemical Vapor Deposition (CVD) Method. *Materials*; 2018.